SIAM J. IMAGING SCIENCES
Vol. 5, No. 4, pp. 1159–1184

Regions of Backprojection and Comet Tail Artifacts for π-Line Reconstruction Formulas in Tomography*

Ryan Hass† and Adel Faridani†

Abstract. We explore two characteristic features of x-ray computed tomography inversion formulas in two and three dimensions that are dependent on π-lines. In such formulas the data from a given source position contribute only to the reconstruction of $f(\mathbf{x})$ for $\mathbf{x}$ in a certain region, called the region of backprojection. The second characteristic is a certain small artifact in the reconstruction called a comet tail artifact. We propose that the comet tail artifact is closely related to the boundary of the region of backprojection and make this relationship precise, developing a general theory of the region of backprojection, its boundary, and the location of the artifact in helical and fan-beam tomography. This theory is applied to a number of specific examples and confirmed by numerical experiments. Furthermore it is demonstrated that a strong comet tail artifact appears in numerical reconstructions from misaligned fan-beam data. A numerical method for using the artifact to find the correct alignment is suggested.

Key words. computed tomography, π-lines, helical tomography, fan-beam tomography

AMS subject classifications. 44A12, 65R10, 92C55

DOI. 10.1137/110857623

1. Introduction.

The advent of exact and feasible inversion formulas for helical x-ray tomography [9, 18, 19] has generated much interest in applications and research. In this paper we investigate two features of these so-called π-line reconstruction formulas and their two-dimensional (2D) analogues [1, 13, 12, 20]. The first is a distinctive feature of π-line reconstruction formulas, namely that data from a given x-ray source position $\mathbf{y}(s)$ contribute only to the reconstruction of $f(\mathbf{x})$ for points $\mathbf{x}$ in a certain region, called the region of backprojection. The second feature is a usually small but characteristic artifact in the reconstruction, called a comet tail artifact, which is illustrated in Figure 1. Here an artifact, originating from the reconstructed smooth function, resembles the appearance of a comet's tail. The size of the error of the comet tail artifact is not large, and it does not affect the rate of convergence of our numerical implementation. In Figure 1 the gray scale is chosen especially to make the artifact clearly visible. Our aim is to better understand why the comet tail artifact occurs and to determine where it will occur.

The paper is organized as follows. In the remainder of this section the definitions and some examples of π-lines, π-intervals, and π-line reconstruction formulas are given.

In section 2 a heuristic principle for determining the location of the comet tail artifact

*Received by the editors December 2, 2011; accepted for publication (in revised form) June 25, 2012; published electronically October 31, 2012. This work was supported by the National Science Foundation under grant DMS-0709495.

http://www.siam.org/journals/siims/5-4/85762.html

†Department of Mathematics, Oregon State University, Corvallis, OR 97331 (hassr@math.oregonstate.edu, faridani@math.oregonstate.edu).

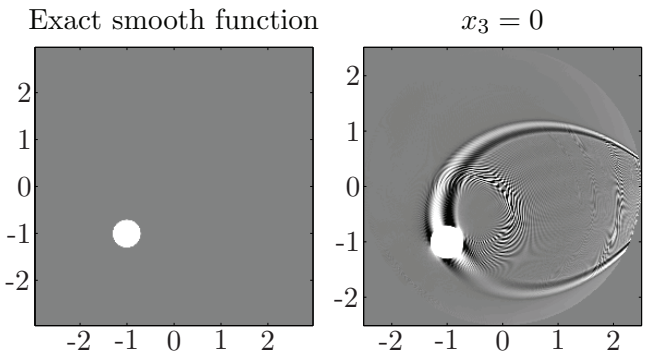

Figure 1. *Left: Original smooth function given by (7.11) with* $\mathbf{x}_0 = (-1, -1, 0)$, $a_1 = .3$, $a_2 = .3$, $a_3 = 2$, $m = 3$, *and* $\psi = 0$. *Displayed in the plane* $x_3 = 0$. *Right: 3D reconstruction by (1.10) displayed in the plane* $x_3 = 0$ *with a comet tail artifact present. The image is displayed with a gray scale* $[-1E-4, 1E-4]$ *in order to highlight the artifact. Reconstruction with parameters* $P = 2560$, $Q = 579$, $D = 6$, $R = 3$, *and* $h = .274/(2\pi)$. *For the meaning of these parameters see (1.1) and section 7.*

is given which relates the location of the artifact to the boundary of the region of backprojection. Then some general properties of the region of backprojection and its boundary are proved which yield a useful reformulation of the heuristic principle and also reveal a close connection between the location of the comet tail artifact and the support of the "Hilbert image" of (1.9) below. The section closes with some specific cases where the general theory simplifies.

Sections 3 and 4 are devoted to specific results and applications in three and two dimensions, respectively. Section 3 details the appearance of the comet tail artifact in three-dimensional (3D) helical tomography. In this case the region of backprojection and its boundary are collections of π-lines. The presentation of the results is greatly eased by the use of certain surfaces of π-lines, called chips in [7], instead of planes.

In section 4 the region of backprojection in 2D fan-beam tomography is constructed for a number of specific families of π-lines, the support of the comet tail artifact is determined according to the theory of section 2, and the results are confirmed with numerical experiments.

If the x-ray data are misaligned, π-line reconstruction formulas yield large comet tail artifacts. In section 5 this particular sensitivity of π-line reconstruction formulas with respect to data misalignment is explored in the 2D case, including the possibility of using this sensitivity to determine the correct data alignment.

A summary and discussion are presented in section 6, and section 7 provides some background on our numerical implementation of the reconstruction formula (1.10) for the experiments presented in this paper.

1.1. π-lines and π-intervals. In x-ray tomography one measures the attenuation of an x-ray beam that passes through the object. The mathematical model used in this paper is given by the divergent beam transform

$$\mathcal{D}f(\mathbf{y}, \boldsymbol{\theta}) = \int_0^\infty f(\mathbf{y} + t\boldsymbol{\theta})\, dt.$$

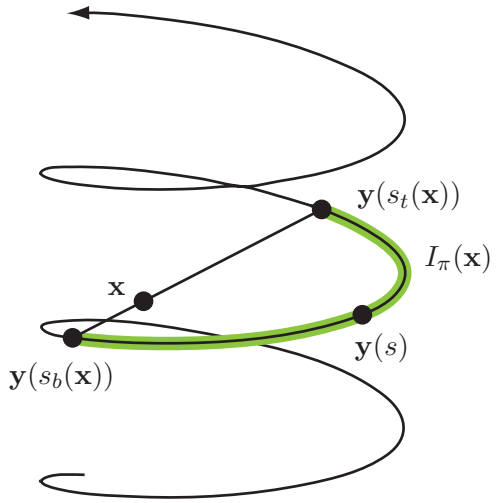

Figure 2. *The π-line for $\mathbf{x}$ is shown as the line segment between $\mathbf{y}(s_b(\mathbf{x}))$ and $\mathbf{y}(s_t(\mathbf{x}))$.*

The function f is the linear x-ray attenuation coefficient of the object, the point $\mathbf{y}$ is the position of the x-ray source, and the unit vector $\boldsymbol{\theta}$ gives the direction of the ray. This model assumes a monochromatic x-ray beam and neglects the effects of scatter and the finite size of both the x-ray tube focal spot and the detector pixel. We assume a mode of data acquisition where the x-ray source moves on a curve $\mathbf{y}(s)$. While π-line reconstruction formulas have also been developed for more general classes of scanning curves [11, 16], in this article the following specific curves are considered. In three dimensions we assume $\mathbf{y}(s)$ to be a helix

$$\mathbf{y}(s) = (R\cos(s), R\sin(s), hs) \tag{1.1}$$

with radius R and pitch h. In two dimensions we assume $\mathbf{y}(s)$ to be a circle with radius R,

$$\mathbf{y}(s) = (R\cos(s), R\sin(s)). \tag{1.2}$$

In the 2D case let S denote the interior of the circle (1.2) and in three dimensions the open helix cylinder $S = \{(x, y, z) \in \mathbf{R}^3 : x^2 + y^2 < R^2\}$ corresponding to (1.1). In both cases we assume the support of f to be contained within S.

Definition 1.1. *Let $L(\mathbf{a}, \mathbf{b})$ denote the line segment connecting points $\mathbf{a}$ and $\mathbf{b}$. A π-line is a line segment $L(\mathbf{y}(s_b), \mathbf{y}(s_t))$ connecting two points $\mathbf{y}(s_b)$, $\mathbf{y}(s_t)$ on the source curve such that $0 < s_t - s_b < 2\pi$. A π-line for a point $\mathbf{x} \in S$ is a π-line $L_\pi(\mathbf{x}) = L(\mathbf{y}(s_b(\mathbf{x})), \mathbf{y}(s_t(\mathbf{x})))$ that contains the point $\mathbf{x}$. We call*

$$I_\pi(\mathbf{x}) = [s_b(\mathbf{x}), s_t(\mathbf{x})]$$

the π-interval or the parametric interval of $\mathbf{x}$.

The condition $0 < s_t - s_b < 2\pi$ means that in the 3D case, $\mathbf{y}(s_b(\mathbf{x}))$ and $\mathbf{y}(s_t(\mathbf{x}))$ are separated by no more than one turn of the helix; cf. Figure 2. The name of the line segment comes from the fact that the data from the source positions on the curve segment between $\mathbf{y}(s_b(\mathbf{x}))$ and $\mathbf{y}(s_t(\mathbf{x}))$ provide views of the point $\mathbf{x}$ over a 180 degree angular range, as is also

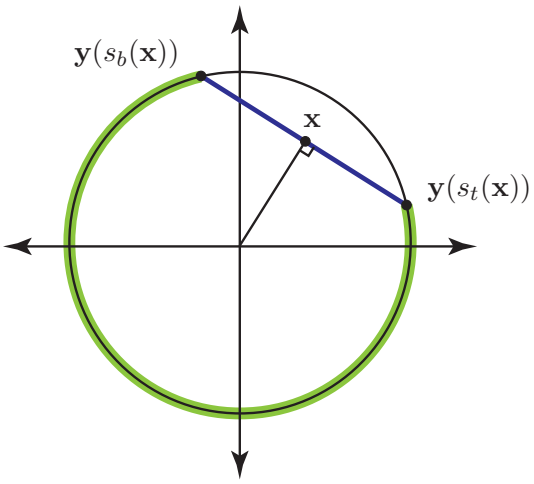

Figure 3. *Orthogonal-long π-lines.*

evident from Figure 2. In two dimensions $\mathbf{y}(s)$ is 2π-periodic, and one identifies s and $s \pm 2\pi$. In this case $I_\pi(\mathbf{x})$ denotes the values of s for which $\mathbf{y}(s)$ lies on the circular arc traversed by beginning at $\mathbf{y}(s_b(\mathbf{x}))$ and moving counterclockwise to $\mathbf{y}(s_t(\mathbf{x}))$.

The following remarkable theorem shows that in the case of the helix the π-lines are uniquely determined.

Theorem 1.2. *Let $\mathbf{y}(s)$ be given by (1.1) and let S be the helix cylinder. Then for any point $\mathbf{x} \in S$ there is a unique π-line containing $\mathbf{x}$.*

Proof. See [2, 7]. ■

On the other hand, in the 2D case with $\mathbf{x}$ in the interior of the circle (1.2), every line through $\mathbf{x}$ would give rise to a π-line for $\mathbf{x}$. We then assume that a specific π-line $L_\pi(\mathbf{x}) = L(\mathbf{y}(s_b(\mathbf{x})), \mathbf{y}(s_t(\mathbf{x})))$ has been selected for each $\mathbf{x}$ and will refer to $L_\pi(\mathbf{x})$ as the π-line of $\mathbf{x}$. We will consider three initial examples.

Orthogonal-long π-lines. The first family of π-lines we consider are *orthogonal-long* π-lines; cf. Figure 3. For the π-line of $\mathbf{x} \in S$ we take the line through $\mathbf{x}$ that is perpendicular to the line segment from the origin to $\mathbf{x}$. The π-line divides the circle into two arcs, and the π-interval of $\mathbf{x}$ is chosen to correspond to the longer arc. Let $\mathbf{x}$ have polar coordinates (ρ, θ); then the orthogonal-long π-line interval is given by

$$s_b(\mathbf{x}) = \theta + \gamma, \quad s_t(\mathbf{x}) = \theta - \gamma, \text{ where } \gamma = \arccos(\rho/R). \tag{1.3}$$

We let $I_\pi(\mathbf{0}) = [-\pi/2, \pi/2]$ and note that $s_b(\mathbf{x})$ and $s_t(\mathbf{x})$ are continuous for $\mathbf{x} \in S \backslash \{\mathbf{0}\}$, but are not continuous at the origin.

Fan-type π-lines. This family of π-lines is given by

$$\begin{aligned} I_\pi(\mathbf{x}) &= [s_b(\mathbf{x}), 2\pi], \\ s_b(\mathbf{x}) &= \pi - 2\alpha^*(0, \mathbf{x}). \end{aligned} \tag{1.4}$$

Here $\alpha^*(0, \mathbf{x})$ denotes the angle between the two rays with vertex $\mathbf{y}(0)$ that pass through $\mathbf{x}$ and through the origin, respectively, as illustrated in Figure 4.

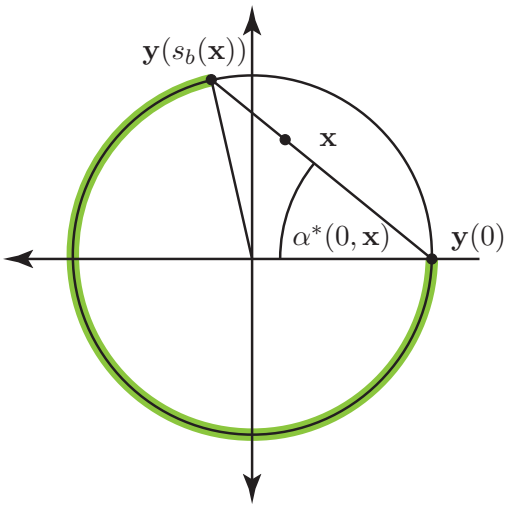

Figure 4. *Construction of fan-type π-lines from* (1.4).

The construction of the π-line at $\mathbf{x}$ follows from Figure 4; that is, one takes the line from $\mathbf{y}(0)$ through $\mathbf{x}$. We call this a *fan-type* family of π-lines.

Parallel π-lines. The third family of π-lines are *parallel* π-lines, where the π-line of $\mathbf{x}$ is given by the line through $\mathbf{x}$ that is parallel to the y-axis. If $\mathbf{x} = (x, y)$, then

$$I_\pi(\mathbf{x}) = [-\alpha, \alpha], \quad \alpha = \arccos(x/R). \tag{1.5}$$

Definition 1.3. *A family of π-lines is called* nonintersecting *if any two π-lines either coincide or do not intersect in S. Equivalently, this means that*

$$\text{for all } \mathbf{x}, \mathbf{x}' \in S: \ \ \mathbf{x} \in L_\pi(\mathbf{x}') \text{ if and only if } \mathbf{x}' \in L_\pi(\mathbf{x}). \tag{1.6}$$

The π-lines of the helix as well as the 2D fan-type and parallel π-lines are nonintersecting, while the orthogonal-long π-lines are not.

1.2. π-line reconstruction formulas.

Definition 1.4. *A π-line reconstruction formula uses for reconstruction at a point $\mathbf{x}$ only data from sources $\mathbf{y}(s)$ with s in the π-interval of $\mathbf{x}$.*

Two fundamental types of π-line reconstruction formulas are backprojection-filtration and filtered backprojection. The backprojection filtration formula can in principle be derived as follows.

Definition 1.5. *For a sufficiently smooth function f of compact support in $\boldsymbol{R}^n$ the Hilbert transform in direction $\boldsymbol{\theta}$ at the point $\mathbf{x}$ is given by*

$$H_{\boldsymbol{\theta}} f(\mathbf{x}) = \frac{1}{\pi} \int_{-\infty}^{\infty} \frac{f(\mathbf{x} - t\boldsymbol{\theta})}{t}\, dt, \tag{1.7}$$

where the integral is understood in the principal value sense.

The following relationship between the Hilbert transform and the divergent beam transform was first found in [4] and later rediscovered and applied to tomography; see, e.g., [19, 18] or [1]. Let

$$\boldsymbol{\beta} = \boldsymbol{\beta}(s, \mathbf{x}) = \frac{\mathbf{x} - \mathbf{y}(s)}{|\mathbf{x} - \mathbf{y}(s)|}. \tag{1.8}$$

Then

$$H_{\boldsymbol{\beta}(s_t(\mathbf{x}),\mathbf{x})} f(\mathbf{x}) = \frac{1}{2\pi} \int_{I_\pi(\mathbf{x})} \frac{1}{|\mathbf{x} - \mathbf{y}(s)|} \frac{\partial}{\partial q} \mathcal{D}f(\mathbf{y}(q), \boldsymbol{\beta}(s, \mathbf{x}))\Big|_{q=s} ds. \tag{1.9}$$

The Hilbert transform on the left-hand side of (1.9) is taken along the π-line of $\mathbf{x}$. In practice it is computed for points $\mathbf{x}$ on a finite segment of a π-line and then needs to be inverted in order to obtain the values of $f(\mathbf{x})$ on that segment. This reconstruction method is known as backprojection-filtration.

Katsevich [9] found an ingenious way to invert by filtering the derivative of the data in a carefully chosen plane before backprojecting. This yields the filtered backprojection formula

$$f(\mathbf{x}) = \frac{1}{2\pi^2} \int_{I_\pi(\mathbf{x})} \frac{1}{|\mathbf{x} - \mathbf{y}(s)|} \int_0^{2\pi} \frac{\partial}{\partial q} \mathcal{D}f(\mathbf{y}(q), \cos\gamma\boldsymbol{\beta} + \sin\gamma\boldsymbol{\beta}^\perp)\Big|_{q=s} \frac{1}{\sin\gamma} d\gamma \, ds, \tag{1.10}$$

where $\boldsymbol{\beta}$ is given again by (1.8).

In three dimensions this is Katsevich's inversion formula [9] for helical tomography. In this case $\boldsymbol{\beta}^\perp$ is defined as follows [9]. For each $s \in I_\pi(\mathbf{x})$ we have a unique $s_2 \in I_\pi(\mathbf{x})$ such that $\mathbf{x}$ lies in a so-called κ-plane that intersects the helix at $\mathbf{y}(s)$, $\mathbf{y}(s_1)$, and $\mathbf{y}(s_2)$, where $s_1 = (s + s_2)/2$. Now $\boldsymbol{\beta}^\perp$ is chosen as a unit vector orthogonal to $\boldsymbol{\beta}$ such that the κ-plane is spanned by $\boldsymbol{\beta}$ and $\boldsymbol{\beta}^\perp$.

Remarkably, both (1.9) and (1.10) also hold in two dimensions. In (1.10) $\boldsymbol{\beta}^\perp$ is in this case given by $\boldsymbol{\beta}^\perp = (-\beta_2, \beta_1)$; cf. [3, Theorem 1]. We always assume the density function f to be sufficiently smooth for (1.9) and (1.10) to hold.

While (1.9) holds for all families of π-lines, using it for the backprojection filtration reconstruction method as described above will be computationally most efficient for families of π-lines that are nonintersecting in the sense of (1.6). On the other hand, the computational efficiency of the filtered backprojection formula (1.10) is not affected by the lack of this property.

2. Region of backprojection. The distinctive feature of π-line reconstruction formulas is that for reconstruction at a point $\mathbf{x}$ only data from source positions from the π-interval of $\mathbf{x}$ are used. Viewed another way, this means that data from a given source position $\mathbf{y}(s)$ contribute only to the reconstruction of $f(\mathbf{x})$ for points $\mathbf{x}$ in a certain region. This region, denoted by $RBP(s)$, is called the region of backprojection for $\mathbf{y}(s)$. In this section we first formulate a heuristic principle for determining the location of the comet tail artifact, which is closely related to the boundary of the region of backprojection. Then a number of general properties of the region of backprojection and its boundary are proved. These allow a useful reformulation of the heuristic principle and also reveal a close connection between the location

of the comet tail artifact and the support of the Hilbert image of (1.9). The following two sections are then devoted to specific results and applications in two and three dimensions, respectively.

Definition 2.1. *We call* $RBP(s) = \{\mathbf{x} \in S \mid s \in I_\pi(\mathbf{x})\}$ *the region of backprojection of position* $\mathbf{y}(s)$. *Let* $\partial RBP(s)$ *denote the boundary of* $RBP(s)$.

A point $\mathbf{x}$ is in the region of backprojection if the current source position is in the point's π-interval. The boundary of $RBP(s)$ is the feature of interest. It represents the cutoff of the points where data from position $\mathbf{y}(s)$ contribute to the reconstruction. This cutoff is the cause of the comet tail artifact, and a heuristic principle for identifying the location of the comet tail artifact can be formulated as follows. Suppose the support of f is a small region around $\mathbf{x}_0$, e.g., f is an approximate δ-function centered at $\mathbf{x}_0$. Then for a given s, the filtered x-ray data will be large for the line connecting $\mathbf{x}_0$ to $\mathbf{y}(s)$, and a contribution to the artifact will occur at the intersection of this line with $\partial RBP(s)$. This motivates the following definition.

Definition 2.2. *For* $\mathbf{x}_0 \in S$ *we define the set* $\Gamma_{\mathbf{x}_0}$ *by*

$$\Gamma_{\mathbf{x}_0} = \{\mathbf{x} \in S \mid \exists s : \mathbf{x} \in \partial RBP(s) \text{ and } \mathbf{x}_0, \mathbf{x}, \text{ and } \mathbf{y}(s) \text{ are collinear}\}. \tag{2.1}$$

Loosely speaking, the points in $\Gamma_{\mathbf{x}_0}$ are where the comet tail artifact would occur if f were given by $f(\mathbf{x}) = \delta(\mathbf{x} - \mathbf{x}_0)$. For a proper function f the location of the full artifact is then given by

$$\Gamma = \bigcup_{\mathbf{x}_0 \in \mathrm{supp}(f)} \Gamma_{\mathbf{x}_0}. \tag{2.2}$$

In order to more easily identify the region of backprojection and $\Gamma_{\mathbf{x}_0}$ for various families of π-lines we now explore some general properties of the region of backprojection and its boundary. These properties of $RBP(s)$ will require continuity of s_b and s_t. Let S_c denote the set

$$S_c = \{\mathbf{x} \in S : s_b \text{ and } s_t \text{ are continuous at } \mathbf{x}\}.$$

Proposition 2.3. *For all* $\mathbf{x} \in S_c$ *one has* $\mathbf{x} \in \partial RBP(s_b(\mathbf{x})) \cup \partial RBP(s_t(\mathbf{x}))$.

The proposition asserts that $\mathbf{x} \in S_c$ cannot lie outside both $\partial RBP(s_b(\mathbf{x}))$ and $\partial RBP(s_t(\mathbf{x}))$.

Before proving Proposition 2.3 we investigate under what conditions one may have $\mathbf{x} \notin \partial RBP(s_b(\mathbf{x}))$ or $\mathbf{x} \notin \partial RBP(s_t(\mathbf{x}))$ for some $\mathbf{x} \in S_c$. An example for $\mathbf{x} \notin \partial RBP(s_t(\mathbf{x}))$ is provided by the fan-type π-lines defined above. Since $s_t(\mathbf{x}) = 2\pi$ for all $\mathbf{x} \in S$, $RBP(2\pi) = S$ and $S \cap \partial RBP(2\pi) = \emptyset$. Thus $\mathbf{x} \notin \partial RBP(s_t(\mathbf{x}))$ for all $\mathbf{x} \in S$.

Lemma 2.4. *Let* $\mathbf{x} \in S_c$. *If* $\mathbf{x} \notin \partial RBP(s_b(\mathbf{x}))$, *then* s_b *has a local maximum at* $\mathbf{x}$. *If* $\mathbf{x} \notin \partial RBP(s_t(\mathbf{x}))$, *then* s_t *has a local minimum at* $\mathbf{x}$.

Proof. Since $s_b(\mathbf{x}) \in I_\pi(\mathbf{x})$, one has $\mathbf{x} \in RBP(s_b(\mathbf{x}))$. If $\mathbf{x} \notin \partial RBP(s_b(\mathbf{x}))$, then there is a neighborhood of $\mathbf{x}$ that is contained in $RBP(s_b(\mathbf{x}))$. This means that for all points $\mathbf{x}'$ in this neighborhood, one has $s_b(\mathbf{x}) \in I_\pi(\mathbf{x}') = [s_b(\mathbf{x}'), s_t(\mathbf{x}')]$. In case of the 3D helix this directly implies $s_b(\mathbf{x}) \geq s_b(\mathbf{x}')$ as desired. In the 2D case the continuity of s_b at $\mathbf{x}$ implies that there is a neighborhood of $\mathbf{x}$ where $|s_b(\mathbf{x}) - s_b(\mathbf{x}')|$ is sufficiently small. In such a neighborhood the condition $s_b(\mathbf{x}) \in I_\pi(\mathbf{x}')$ does imply $s_b(\mathbf{x}) \geq s_b(\mathbf{x}')$. In this context we understand $s_b(\mathbf{x}) \geq s_b(\mathbf{x}')$ in the sense that $\mathbf{y}(s_b(\mathbf{x}))$ is obtained from $\mathbf{y}(s_b(\mathbf{x}'))$ by a small counterclockwise rotation. The proof for s_t is entirely analogous. ∎

We now present the proof of Proposition 2.3.

Proof. We first show that in the case of the helix the functions $s_b(\mathbf{x}), s_t(\mathbf{x})$ have no local extrema. The assertion then follows from Lemma 2.4 and the continuity proved in Lemma 3.5 at the end of section 3. Let $\mathbf{x}_0 \in S$ be arbitrary and let $t = (s_b(\mathbf{x}_0) + s_t(\mathbf{x}_0))/2$ and $\alpha = (s_t(\mathbf{x}_0) - s_b(\mathbf{x}_0))/2$. Then $I_\pi(\mathbf{x}_0) = [t-\alpha, t+\alpha]$ with $0 < \alpha < \pi$ and $\mathbf{x}_0 \in L(\mathbf{y}(t-\alpha), \mathbf{y}(t+\alpha)) = L_\pi(\mathbf{x}_0)$. Let U be any open neighborhood of $\mathbf{x}_0$. Because of the continuity of the helical curve $\mathbf{y}(s)$ there are α_-, α_+ sufficiently close to α with $0 < \alpha_- < \alpha < \alpha_+ < \pi$ such that the line segments $L_- = L(\mathbf{y}(t-\alpha_-), \mathbf{y}(t+\alpha_-))$ and $L_+ = L(\mathbf{y}(t-\alpha_+), \mathbf{y}(t+\alpha_+))$ intersect U. Let $\mathbf{x}_\pm \in L_\pm \cap U$, respectively. Both L_+ and L_- are π-lines, and according to Theorem 1.2 one has $L_\pm = L_\pi(\mathbf{x}_\pm)$, respectively. Because of $t - \alpha_+ = s_b(\mathbf{x}_+) < t - \alpha = s_b(\mathbf{x}_0) < t - \alpha_- = s_b(\mathbf{x}_-)$ and $t + \alpha_- = s_t(\mathbf{x}_-) < t + \alpha = s_t(\mathbf{x}_0) < t + \alpha_+ = s_t(\mathbf{x}_+)$, it follows that neither $s_b(\mathbf{x})$ nor $s_t(\mathbf{x})$ can have a local extremum at $\mathbf{x}_0$.

We now turn to the 2D case where the curve $\mathbf{y}(s)$ is the circle (1.2) and S its interior. Let $\mathbf{x}_0 \in S_c$ be arbitrary, $\boldsymbol{\beta} = (\beta_1, \beta_2)$ the unit vector in direction of $\mathbf{x}_0 - \mathbf{y}(s_b(\mathbf{x}_0))$, and $\boldsymbol{\beta}^\perp = (-\beta_2, \beta_1)$. That is, $\boldsymbol{\beta}^\perp$ is obtained by rotating $\boldsymbol{\beta}$ by 90 degrees counterclockwise. Note that $\boldsymbol{\beta}$ is parallel and $\boldsymbol{\beta}^\perp$ perpendicular to $L_\pi(\mathbf{x}_0)$. The π-line $L_\pi(\mathbf{x}_0)$ divides $\overline{S}$, the closure of S, into two disjoint parts S_+ and S_- given by

$$S_+ = \{\mathbf{x} \in \overline{S} : (\mathbf{x} - \mathbf{x}_0) \cdot \boldsymbol{\beta}^\perp \geq 0\},$$
$$S_- = \{\mathbf{x} \in \overline{S} : (\mathbf{x} - \mathbf{x}_0) \cdot \boldsymbol{\beta}^\perp < 0\}.$$

Assume that $\mathbf{x}_0 \notin \partial RBP(s_b(\mathbf{x}_0)) \cup \partial RBP(s_t(\mathbf{x}_0))$. According to Lemma 2.4 this implies that s_b has a local maximum and s_t a local minimum at $\mathbf{x}_0$. Hence there is an open neighborhood U of $\mathbf{x}_0$ such that $s_b(\mathbf{x}) \leq s_b(\mathbf{x}_0)$ and $s_t(\mathbf{x}) \geq s_t(\mathbf{x}_0)$ for all $\mathbf{x} \in U$. This implies that both $\mathbf{y}(s_b(\mathbf{x}))$ and $\mathbf{y}(s_t(\mathbf{x}))$ lie in S_+ for all $\mathbf{x} \in U$. Since S_+ is convex, the π-lines $L_\pi(\mathbf{x}) = L(\mathbf{y}(s_b(\mathbf{x})), \mathbf{y}(s_t(\mathbf{x})))$ lie entirely in S_+ for all $\mathbf{x} \in U$. But this is a contradiction since U does contain points in S_-. ∎

Proposition 2.5. *Suppose* $\mathbf{x} \in S_c \cap \partial RBP(s)$. *Then* $\mathbf{x} \in RBP(s)$ *and* $s = s_b(\mathbf{x})$ *or* $s = s_t(\mathbf{x})$. *In particular, the line segment from* $\mathbf{x}$ *to* $\mathbf{y}(s)$ *is contained in the* π*-line of* $\mathbf{x}$.

Proof. Suppose $\mathbf{x} \in S_c$ lies outside $RBP(s)$, that is, $s \notin I_\pi(\mathbf{x}) = [s_b(\mathbf{x}), s_t(\mathbf{x})]$. Since I_π is closed and s_b and s_t are continuous at $\mathbf{x}$, the condition $s \notin I_\pi(\mathbf{x}')$ must then also hold for all $\mathbf{x}'$ in some open neighborhood of $\mathbf{x}$. Hence, if $\mathbf{x} \in S_c \cap \partial RBP(s)$, then $\mathbf{x} \in RBP(s)$. Similarly, the continuity of s_b and s_t at $\mathbf{x}$ implies that if $\mathbf{x} \in S_c \cap RBP(s)$ and s lies in the interior of $I_\pi(\mathbf{x})$, then s will also lie in the interior of $I_\pi(\mathbf{x}')$ for all $\mathbf{x}'$ in some open neighborhood of $\mathbf{x}$. Hence this neighborhood is contained in $RBP(s)$, so $\mathbf{x}$ does not lie on the boundary of $RBP(s)$. It follows that if $\mathbf{x} \in S_c \cap \partial RBP(s)$, then either $s = s_b(\mathbf{x})$ or $s = s_t(\mathbf{x})$. In either case, the line segment from $\mathbf{x}$ to $\mathbf{y}(s)$ is contained in the π-line of $\mathbf{x}$. ∎

The next proposition provides a useful characterization of $\Gamma_{\mathbf{x}_0} \cap S_c$.

Proposition 2.6. *For all* $\mathbf{x}_0 \in S$ *one has*

$$\Gamma_{\mathbf{x}_0} \cap S_c \;=\; \{\mathbf{x} \in S_c \mid \mathbf{x}_0 \in L_\pi(\mathbf{x})\}. \tag{2.3}$$

Proof. Let $\mathbf{x}_0 \in S$ be arbitrary. If $\mathbf{x} \in \Gamma_{\mathbf{x}_0}$, then by (2.1) there is s such that $\mathbf{x} \in \partial RBP(s)$ and $\mathbf{x}, \mathbf{x}_0$ and $\mathbf{y}(s)$ are collinear. If in addition $\mathbf{x} \in S_c$, it follows from Proposition 2.5 that

$L_\pi(\mathbf{x})$ contains both $\mathbf{x}$ and $\mathbf{y}(s)$, and therefore also $\mathbf{x}_0$. On the other hand, for all $\mathbf{x} \in S_c$ it follows from (2.1) and Proposition 2.3 that if $\mathbf{x}_0 \in L_\pi(\mathbf{x})$, then $\mathbf{x} \in \Gamma_{\mathbf{x}_0}$. ■

As an immediate consequence one obtains the following characterization of the support of the comet tail artifact.

Corollary 2.7. *A point $\mathbf{x} \in S_c$ lies in the support Γ of the comet tail artifact if and only if its π-line intersects the support of f.*

Proof. With the set Γ as given by (2.2) and using Proposition 2.6 one has

$$\begin{aligned}\Gamma \cap S_c &= \bigcup_{\mathbf{x}_0 \in \operatorname{supp}(f)} \Gamma_{\mathbf{x}_0} \cap S_c \\ &= \bigcup_{\mathbf{x}_0 \in \operatorname{supp}(f)} \{\mathbf{x} \in S_c : \mathbf{x}_0 \in L_\pi(\mathbf{x})\} \\ &= \{\mathbf{x} \in S_c : L_\pi(\mathbf{x}) \cap \operatorname{supp}(f) \neq \emptyset\}. \qquad (2.4)\end{aligned}$$

■

This in turn reveals a close connection to the support of the Hilbert image $H_{\boldsymbol{\beta}(s_t(\mathbf{x}),\mathbf{x})} f(\mathbf{x})$ of (1.9).

Corollary 2.8. *Let $g(\mathbf{x}) = H_{\boldsymbol{\beta}(s_t(\mathbf{x}),\mathbf{x})} f(\mathbf{x})$ and $\mathbf{x} \in S_c$. If $\mathbf{x} \notin \Gamma$, then $g(\mathbf{x}) = 0$.*

Proof. It follows from (1.9) that $g(\mathbf{x}) = 0$ if the π-line of $\mathbf{x}$ does not intersect the support of f. The assertion then follows from Corollary 2.7. ■

We conclude this section with some simplifications that occur for families of π-lines with special properties.

Corollary 2.9. *Let the family of π-lines $L_\pi(\mathbf{x}), \mathbf{x} \in S$ be nonintersecting. Then*

$$\Gamma_{\mathbf{x}_0} \cap S_c = L_\pi(\mathbf{x}_0) \cap S_c \qquad (2.5)$$

for all $\mathbf{x}_0 \in S$. Consequently, $\Gamma \cap S_c$ equals the intersection of S_c with the union of all π-lines that intersect the support of f.

Proof. It follows from the hypothesis that $\mathbf{x}_0 \in L_\pi(\mathbf{x})$ if and only if $\mathbf{x} \in L_\pi(\mathbf{x}_0)$. The assertion now follows from Proposition 2.6 and (2.2). ■

It has already been mentioned that the fan-type π-lines are an example of where the converse of Proposition 2.5 does not hold. We call those families of π-lines for which it does hold boundary-regular.

Definition 2.10. *A family of π-lines is called* boundary-regular *if*

$$\begin{aligned}\text{for all } \mathbf{x} \in S_c: \quad \mathbf{x} \in \partial RBP(s) &\Leftrightarrow s \in \{s_b(\mathbf{x}), s_t(\mathbf{x})\} \\ &\Leftrightarrow \mathbf{y}(s) \in L_\pi(\mathbf{x}).\end{aligned}$$

It follows from Lemma 2.4 and Proposition 2.5 that a family of π-lines will be boundary-regular if s_b has no local maxima and s_t no local minima in S_c. For the helix these conditions were verified in the proof of Proposition 2.3, so the π-lines of the helix are boundary-regular. It is easy to see, as shown in the next section, that the orthogonal-long and parallel π-lines are also boundary-regular, while we have already seen that the fan-type π-lines are not.

Proposition 2.11. *Let the family of π-lines $L_\pi(\mathbf{x})$, $\mathbf{x} \in S$, be nonintersecting and boundary-regular. Then $S_c \cap \partial RBP(s)$ equals the intersection of S_c with the union of all π-lines that contain $\mathbf{y}(s)$.*

Proof. Let $M(s)$ denote the union of all π-lines $L_\pi(\mathbf{x}')$, $\mathbf{x}' \in S$, that contain $\mathbf{y}(s)$. It follows immediately from Proposition 2.5 that $S_c \cap \partial RBP(s) \subseteq M(s)$. Now assume $\mathbf{x} \in S_c \cap M(s)$. Then there is $\mathbf{x}' \in S$ such that $L_\pi(\mathbf{x}')$ contains both $\mathbf{x}$ and $\mathbf{y}(s)$. Since the family of π-lines is nonintersecting, $L_\pi(\mathbf{x}') = L_\pi(\mathbf{x})$. Hence $\mathbf{y}(s) \in L_\pi(\mathbf{x})$, so $s \in \{s_b(\mathbf{x}), s_t(\mathbf{x})\}$. Since the family of π-lines is boundary-regular, it follows that $\mathbf{x} \in \partial RBP(s)$. ∎

3. Helical scanning trajectories. In this section we describe the support of the comet tail artifact and the region of backprojection for the 3D helical scanning trajectory. The source curve is the helix (1.1); i.e., $\mathbf{y}(s) = (R\cos(s), R\sin(s), hs)$ and S now denotes the helix cylinder $S = \{(x, y, z) \in \mathbf{R}^3 : x^2 + y^2 < R^2\}$.

Theorem 3.1. *The family of π-lines for the helix is nonintersecting and boundary-regular with $S_c = S$. $\partial RBP(s) \cap S$ equals the intersection of S with the union of all π-lines that contain $\mathbf{y}(s)$. The set $\Gamma_{\mathbf{x}_0} \cap S$ is given by the intersection of S with the π-line of $\mathbf{x}_0$, and the support Γ of the comet tail artifact equals the intersection of S with the union of all π-lines that intersect the support of f.*

Proof. Theorem 1.2 implies that the π-lines are nonintersecting. It follows from Lemma 2.4 and Proposition 2.5 that a family of π-lines will be boundary-regular if s_b has no local maxima and s_t no local minima in S_c. For the helix these conditions were verified in the proof of Proposition 2.3, so the π-lines of the helix are boundary-regular. Lemma 3.5, proved at the end of this section, gives $S_c = S$. The remaining assertions now follow from Corollary 2.9 and Proposition 2.11. ∎

As observed in [15], the π-lines containing $\mathbf{y}(s)$ form an upper surface S_U and a lower surface S_L given by

$$S_U = \bigcup_{0<\alpha<2\pi} L(\mathbf{y}(s), \mathbf{y}(s+\alpha)),$$
$$S_L = \bigcup_{0<\alpha<2\pi} L(\mathbf{y}(s-\alpha), \mathbf{y}(s))$$

so that

$$\partial RBP(s) = S_U \cup S_L.$$

The region of backprojection RBP(s) is then the region between these two surfaces. Furthermore, the symmetry of the helix implies that $RBP(s)$ will be a rotated and translated copy of $RBP(0)$.

The intersections of the region of backprojection and of the support of the comet tail artifact with a plane turn out to be somewhat complicated. For example, as seen in Figure 5, $RBP(s) \cap \{x_3 = 0\}$ changes its size and shape as s varies. Similarly, the simple structure of the support of the comet tail artifact being a union of π-lines is not readily apparent from its intersection with the plane $x_3 = 0$ as shown in Figure 1 (right) and also in Figure 7 (left) below. Nevertheless, an analytical expression for the intersection of ∂RBP with a horizontal plane can be given.

Proposition 3.2. *Let $\mathbf{y}(s)$ denote the helix $\mathbf{y}(s) = (R\cos s, R\sin s, hs)$ and $\Pi(s_0)$ the plane $x_3 = hs_0$. Let*

$$K_s(t) = \frac{1}{s-t}((s-s_0)\mathbf{y}(t) - (t-s_0)\mathbf{y}(s)).$$

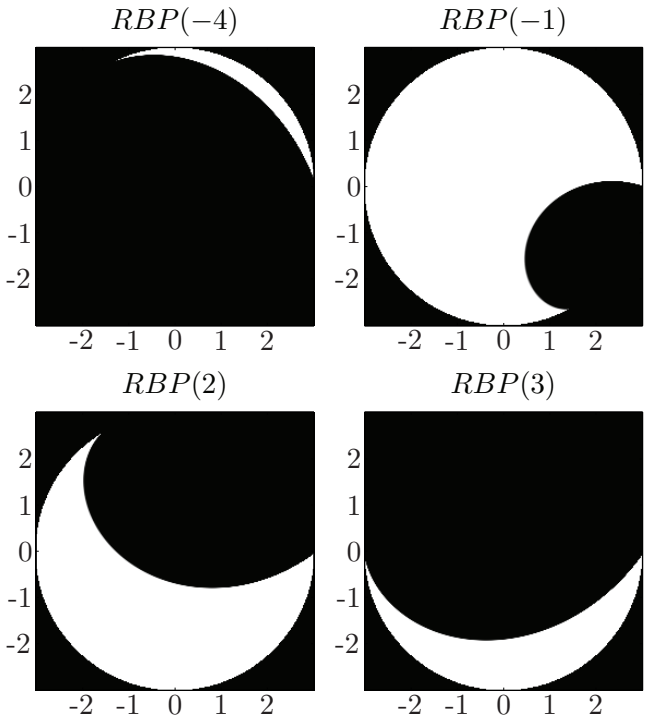

Figure 5. *Region of backprojection for the 3D formula (white) for helix π-lines for the plane $x_3 = 0$ with $R = 3$.*

Then

$$\partial RBP(s) \cap \Pi(s_0) \cap S = \begin{cases} \{K_s(t),\ s - 2\pi < t < s_0\} & \text{if } s_0 < s < s_0 + 2\pi, \\ \{K_s(t),\ s_0 < t < s + 2\pi\} & \text{if } s_0 - 2\pi < s < s_0. \end{cases} \tag{3.1}$$

Proof. $\partial RBP(s)$ is the union of all π-lines that pass through $\mathbf{y}(s)$. The intersection of this family of π-lines with the plane $\Pi(s_0)$ defines the desired curve. Let $s_0 < s < s_0 + 2\pi$. A π-line passing through $\mathbf{y}(s)$ and intersecting $\Pi(s_0)$ will intersect the source curve at a point $\mathbf{y}(t)$ for $s - 2\pi \le t \le s_0$. The line segment connecting $\mathbf{y}(s)$ and $\mathbf{y}(t)$ is given by

$$(1-u)\mathbf{y}(s) + u\mathbf{y}(t), \quad 0 \le u \le 1.$$

This line segment intersects the plane $\Pi(s_0)$ for the value of u for which $(1-u)hs + uht = hs_0$, that is, for $u = (s - s_0)/(s - t)$. This gives

$$(1-u)\mathbf{y}(s) + u\mathbf{y}(t) = \frac{1}{s-t}\left((s_0 - t)\mathbf{y}(s) + (s - s_0)\mathbf{y}(t)\right) = K_s(t).$$

The case of $s_0 - 2\pi < s < s_0$ follows in the same way. ∎

One observes that the endpoints of the curve (3.1) are $K_s(s_0) = \mathbf{y}(s_0)$ and $K_s(s \pm 2\pi) = (R\cos(s), R\sin(s), hs_0)$, the latter being the orthogonal projection of $\mathbf{y}(s)$ onto $\Pi(s_0)$. The curve divides $S \cap \Pi(s_0)$ into two regions. The region not containing the line connecting the two endpoints is $RBP(s) \cap \Pi(s_0)$; cf. Figure 5.

More insight can be gained from studying the intersections of the region of backprojection and the artifact with the following surfaces, called chips, that are unions of π-lines and are adapted to the geometry of the helix.

Definition 3.3. *The chip anchored at $\mathbf{y}(t)$, denoted by $C(t)$, is the portion within the helix cylinder S of the union of all π-lines with endpoints equidistant along the helix from $\mathbf{y}(t)$. That is,*

$$\begin{aligned} C(t) &= S \cap \bigcup_{\alpha\in(0,\pi)} L(\mathbf{y}(t-\alpha),\mathbf{y}(t+\alpha)) \\ &= \{\mathbf{x}\in S | I_\pi(\mathbf{x}) = [t-\alpha, t+\alpha], \alpha\in(0,\pi)\}. \end{aligned} \tag{3.2}$$

The line joining $\mathbf{y}(t)$ to $(0,0,ht)$ is called the chip axis.

Chips were originally introduced in [7] and used in an algorithm to calculate the π-interval endpoints for any point in S. It was shown in [7] that every point in S belongs to a unique chip $C(t)$ and that

$$(\mathbf{y}(t+\alpha)-\mathbf{y}(t-\alpha))\cdot((0,0,ht)-\mathbf{y}(t)) = 0, \tag{3.3}$$

i.e., all π-lines in a chip are orthogonal to the chip axis. Chips are also very convenient for implementing the backprojection-filtration reconstruction method based on (1.9); cf. [5].

The intersection of $RBP(s)$ with chip $C(t)$ is now conveniently described.

Lemma 3.4. *Let $C(t)$ be the chip anchored at t. Then*

$$RBP(s)\cap C(t) \;=\; S\cap \bigcup_{|t-s|\le\alpha<\pi} L(\mathbf{y}(t-\alpha),\mathbf{y}(t+\alpha))$$

and

$$\partial RBP(s)\cap C(t) = S\cap L(\mathbf{y}(t-\alpha_0),\mathbf{y}(t+\alpha_0)), \quad \alpha_0 = |t-s| < \pi. \tag{3.4}$$

Proof.

$$\begin{aligned} RBP(s)\cap C(t) &= \{\mathbf{x}\in C(t) \mid s\in I_\pi(\mathbf{x})\} \\ &= \{\mathbf{x}\in C(t) \mid I_\pi(\mathbf{x}) = [t-\alpha,t+\alpha], |t-s|\le\alpha<\pi\}, \\ &= S\cap \bigcup_{|t-s|\le\alpha<\pi} L(\mathbf{y}(t-\alpha),\mathbf{y}(t+\alpha)); \end{aligned}$$

see also Figure 9. Furthermore,

$$\begin{aligned} \mathbf{x}\in C(t)\cap\partial RBP(s) &\Leftrightarrow \mathbf{x}\in C(t) \text{ and } s\in\{s_b(\mathbf{x}),\, s_t(\mathbf{x})\} \\ &\Leftrightarrow I_\pi(\mathbf{x}) = [t-\alpha_0, t+\alpha_0],\ 0<\alpha_0 = |t-s|<\pi. \end{aligned}$$ ∎

If, for example, $s < t$, then according to (3.4) the intersection of the boundary of the region of backprojection $RBP(s)$ with the chip $C(t)$ is the π-line from $\mathbf{y}(s)$ to $\mathbf{y}(2t-s)$.

As s increases from $t-\pi$ to $t+\pi$, the region of backprojection for the chip $C(t)$ expands from $\mathbf{y}(t-\pi)$ to the chip's anchor point $\mathbf{y}(t)$ and then retracts, as illustrated in Figure 6.

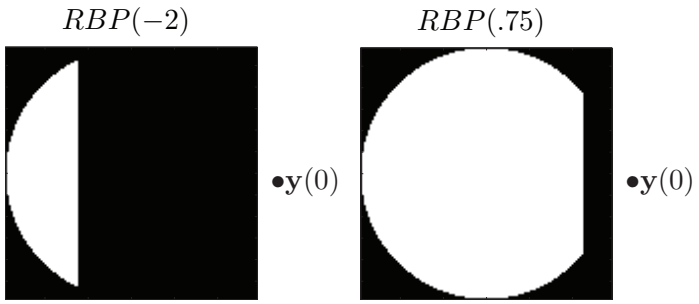

Figure 6. *On each chip, $RBP(s)$ expands toward the anchor point and then retracts as s traverses the interval $[t-\pi, t+\pi]$. Shown is $RBP(s) \cap C(0)$.*

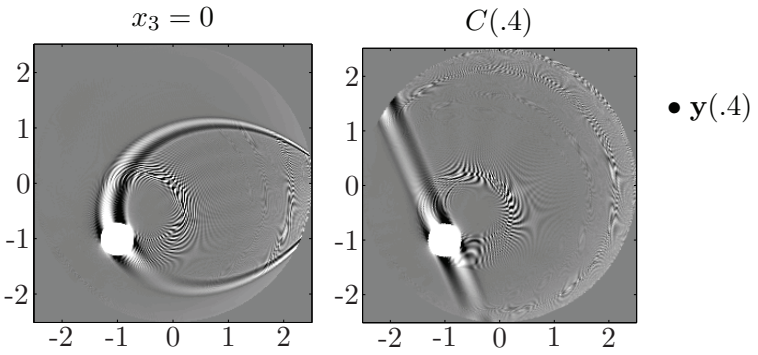

Figure 7. *Left: 3D reconstruction with (1.10) in the plane $x_3 = 0$. The reconstructed function is (7.11) with $\mathbf{x}_0 = (-1, -1, 0)$, $a_1 = .3$, $a_2 = .3$, $a_3 = 2$, $m = 3$, and $\psi = 0$. Reconstructed with $P = 2560$, $Q = 579$, $R = 3$, $D = 6$, and $p = .274$. The image grayscale range is $[-1E-4, 1E-4]$. Right: Same function as before but reconstructed on the chip $C(.4)$.*

Figure 7 (right) shows the reconstruction on the chip $C(.4)$ instead of the plane $x_3 = 0$. Now the structure of the support Γ of the artifact as the set of all π-lines that pass through the support of the function is readily apparent. Here the π-lines on the chip $C(.4)$ are orthogonal to the chip axis that passes through the point $\mathbf{y}(.4)$ as shown in (3.3).

The reconstructions shown in this paper are based on the filtered backprojection formula (1.10) as described in section 7 below. In particular, the backprojection step has been implemented using formulas (63) and (64) in [14]. The images shown in Figure 8 demonstrate that the comet tail artifact does not depend on this one particular discretization of the backprojection step and also occurs in reconstructions with the backprojection-filtration approach. Figure 8 (left) shows the same reconstruction as in Figure 7 (left), except that the backprojection has been implemented differently, this time according to formulas (57) and (58) in [14] instead of formulas (63) and (64). Figure 8 (right) corresponds to Figure 7 (right), the reconstruction being done this time with the backprojection-filtration approach. In both cases the comet tail artifact remains present at the expected locations.

We conclude this section by proving the continuity of s_b and s_t.

Lemma 3.5. *For the helix, $s_b(\mathbf{x})$ and $s_t(\mathbf{x})$ are continuous functions of $\mathbf{x} \in S$.*

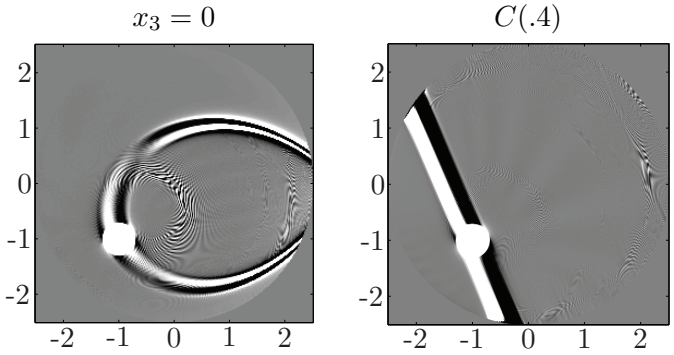

Figure 8. *Left: Same image as in Figure 7 (left) but reconstructed with an alternative discretization of the backprojection. Right: Reconstruction on the chip $C(.4)$ from the same data as in Figure 7 (right) but with the backprojection-filtration approach.*

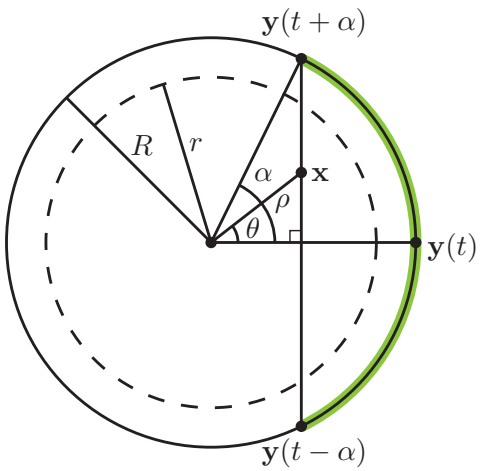

Figure 9. *$C(t)$ projected onto the xy-plane.*

Proof. As shown in [7], every point in S belongs to a unique chip $C(t)$, and each point $\mathbf{x} \in C(t)$ may be written as

$$\mathbf{x} = \left(\rho\cos(\theta+t), \rho\sin(\theta+t), h\left(t + \frac{(\rho/R)\sin\theta\cos^{-1}\left((\rho/R)\cos\theta\right)}{\sqrt{1-(\rho/R)^2\cos^2\theta}}\right)\right) \tag{3.5}$$

for some $0 \le \rho < R$, $\theta \in [-\pi, \pi)$; cf. Figure 9. Thus the chips provide a natural decomposition of S and introduce a new coordinate system (t, ρ, θ).

Now let $\mathbf{x} \in C(t)$ with chip coordinates (t, ρ, θ) with respect to the representation (3.5). Suppose $\mathbf{x}_n \to \mathbf{x}$ where $\mathbf{x}_n$ has chip coordinates (t_n, ρ_n, θ_n). It follows from (3.5) that as $n \to \infty$, $(t_n, \rho_n, \theta_n) \to (t, \rho, \theta)$, provided that $\rho, \rho_n < R$ for all n.

Now $s_b(\mathbf{x}) = t - \alpha = t - \arccos(\rho\cos(\theta))$; cf. Figure 9. Let $\mathbf{z}_n \in C(t)$ with chip coordinates (t, ρ_n, θ_n). Then $|s_b(\mathbf{x}) - s_b(\mathbf{x}_n)| \le |s_b(\mathbf{x}) - s_b(\mathbf{z}_n)| + |s_b(\mathbf{z}_n) - s_b(\mathbf{x}_n)| = |\arccos(\rho\cos(\theta)) - \arccos(\rho_n\cos(\theta_n))| + |t - t_n|$. Hence $|s_b(\mathbf{x}) - s_b(\mathbf{x}_n)| \to 0$ as $n \to \infty$. The continuity of s_t can be shown in the same way. ∎

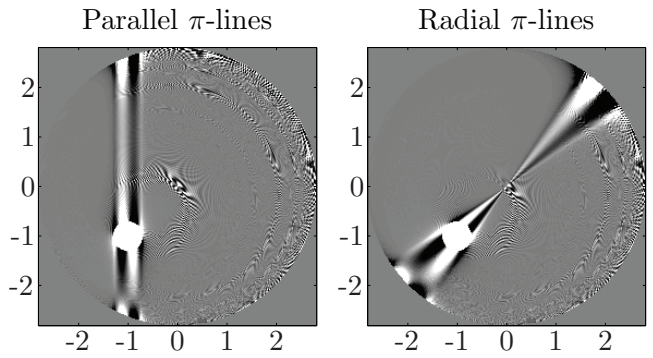

Figure 10. *Left: Comet tail artifact for parallel π-lines. Right: Comet tail artifact for radial π-lines. Both images reconstructed using formula (1.10) in the form (7.5) with $P = 2560$, $Q = 668$, $R = 3$, and $D = 6$. The image grayscale range is $[-8E-5, 8E-5]$, chosen to display the artifact. The reconstructed function is (7.11) with $\mathbf{x}_0 = (-1,-1)$, $a_1 = .3$, $a_2 = .3$, $m = 3$, and $\psi = 0$.*

4. Fan-beam geometry. This section is devoted to the 2D case, with $\mathbf{y}(s)$ given by the circle (1.2) and S the interior of the circle. In the following we examine the region of backprojection and the support of the comet tail artifact for several families of π-lines.

For the *parallel* π-lines defined by (1.5) it is easy to see that they are nonintersecting and that s_b and s_t are continuous in S and have no local extrema. So the family is boundary-regular and $S_c = S$. By Proposition 2.11, $\partial RBP(s)$ is the intersection of S with the π-line containing $\mathbf{y}(s)$, that is, with the vertical line passing through $\mathbf{y}(s)$. By the definition (1.5) of the π-intervals, $RBP(s)$ is the part of S to the left of that line, i.e., $RBP(s) = \{(x,y) \in S \mid x \le R\cos(s)\}$. As s increases from $-\pi$ to π, the region of backprojection expands from the left toward the point $(R,0)$ and then retracts. We have seen similar behavior with the helix chips in section 3; cf. Figures 6 and 9. By Corollary 2.9 the comet tail artifact appears along all π-lines that intersect the support of f. The numerical experiment shown in Figure 10 (left) confirms this finding.

The *radial* π-lines are given by taking the line through $\mathbf{x}$ and the origin, together with the π-interval $[\theta, \theta+\pi]$, where θ is the polar angle of $\mathbf{x}$. For $\mathbf{x} = 0$ we choose the x-axis as the π-line with the π-interval $[0,\pi]$. This family of π-lines is boundary-regular with $S_c = S\backslash\{\mathbf{0}\}$. The nonintersection property (1.6) holds for $\mathbf{x}, \mathbf{x}' \neq \mathbf{0}$. It follows by direct inspection that $S_c \cap RBP(s)$ is the intersection of S_c with the half-plane $\mathbf{x}\cdot\mathbf{y}(s)^{\perp} \le \mathbf{0}$, where $\mathbf{y}(s)^{\perp}$ equals $\mathbf{y}(s)$ rotated counterclockwise by 90 degrees. Hence $\partial RBP(s)$ equals the intersection of S with the line through $\mathbf{y}(s)$ and the origin. The origin itself is always contained in $\partial RBP(s)$ but lies in $RBP(s)$ only for the values $s \in I_\pi(\mathbf{0}) = [0,\pi]$. By (2.1) one has for $\mathbf{x}_0 \neq \mathbf{0}$ that $\Gamma_{\mathbf{x}_0} = S \cap L_\pi(\mathbf{x}_0)$ and $\Gamma_{\mathbf{0}} = S$. The comet tail artifact will thus appear along all π-lines that intersect the support of f, which is illustrated in the numerical experiment in Figure 10 (right). If the support of f contains the origin, then the artifact will appear everywhere in S.

For the *fan-type* π-lines one has $S_c = S$ and $RBP(0) = S$. For $s \neq 0$ the line segment $L(\mathbf{y}(0), \mathbf{y}(s))$ divides S into two regions; cf. Figure 4. It follows directly from (1.4) that $RBP(s)$ corresponds to the region bounded by this line segment and the arc $\{\mathbf{y}(t), 0 \le t \le s\}$. Since the fan-type π-lines are nonintersecting, according to Corollary 2.9 the comet tail artifact will again appear along all π-lines that intersect the support of f.

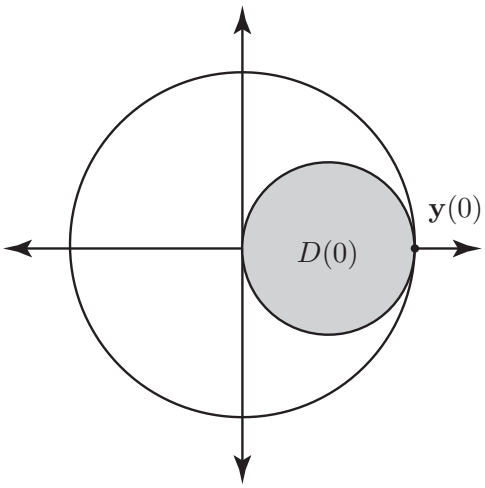

Figure 11. *The region of backprojection for orthogonal-long π-lines is the region inside S and outside the open disk $D(s) = \{\mathbf{x} : |\mathbf{x} - \mathbf{y}(s)/2| < R/2\}$, shown here for $s = 0$. The exceptional point $\mathbf{x} = \mathbf{0}$ lies in $RBP(s)$ only for $s \in I_\pi(\mathbf{0}) = [-\pi/2, \pi/2]$.*

The next few families of π-lines lack the nonintersection property, and determination of $RBP(s)$ and Γ is less immediate. We begin with the *orthogonal-long* π-lines.

Theorem 4.1. *The orthogonal-long family is boundary-regular with $S_c = S\backslash\{\mathbf{0}\}$. The set $\Gamma_{\mathbf{x}_0}$ is the circle centered at $\mathbf{x}_0/2$ with radius $|\mathbf{x}_0/2|$. The region of backprojection is given by*

$$RBP(s) \cap S_c = \{\mathbf{x} \in S_c : |\mathbf{x} - \mathbf{y}(s)/2| \geq R/2\};$$

cf. Figure 11. The exceptional point $\mathbf{x} = \mathbf{0}$ lies on $\partial RBP(s)$ for all s, in $RBP(s)$ for $s \in I_\pi(\mathbf{0}) = [-\pi/2, \pi/2]$, and in $\Gamma_{\mathbf{x}_0}$ for all $\mathbf{x}_0 \in S$.

We first establish an auxiliary result about the nesting of orthogonal-long π-intervals.

Lemma 4.2. *Let $0 < t < 1$ and $\mathbf{0} \neq \mathbf{x} \in S$. Then $I_\pi(t\mathbf{x}) \subsetneq I_\pi(\mathbf{x})$.*

Proof. Let $\mathbf{x}$ have polar coordinates (ρ, θ). Recall that the orthogonal-long π-intervals are defined by (1.3), i.e., $s_b(\mathbf{x}) = \theta + \gamma$ and $s_t(\mathbf{x}) = \theta - \gamma$, where $\gamma = \arccos(\rho/R)$. Hence $s_b(t\mathbf{x}) = \theta + \arccos(t\rho/R) > \theta + \arccos(\rho/R) = s_b(\mathbf{x})$ and $s_t(t\mathbf{x}) = \theta - \arccos(t\rho/R) < \theta - \arccos(\rho/R) = s_t(\mathbf{x})$. Thus $I_\pi(t\mathbf{x}) \subsetneq I_\pi(\mathbf{x})$. ∎

We can now prove Theorem 4.1.

Proof. It follows directly from (1.3) that $S_c = S\backslash\{\mathbf{0}\}$. Lemma 4.2 implies that s_b and s_t have no local extrema in S_c, so by Lemma 2.4 and Proposition 2.5 the orthogonal-long π-lines are boundary-regular. Because of boundary-regularity one has for $\mathbf{x} \neq \mathbf{0}$

$$\mathbf{x} \in \partial RBP(s) \Leftrightarrow \mathbf{y}(s) \in L_\pi(\mathbf{x}) \Leftrightarrow \mathbf{x} \perp (\mathbf{x} - \mathbf{y}(s)) \Leftrightarrow |\mathbf{x} - \mathbf{y}(s)/2| = |\mathbf{y}(s)|/2.$$

The orthogonality of $\mathbf{x}$ and $(\mathbf{x} - \mathbf{y}(s))$ comes from the π-lines being orthogonal to $\mathbf{x}$ for this family. The last equivalence is evident from the calculation

$$|\mathbf{x} - \mathbf{y}(s)/2|^2 \;=\; \mathbf{x} \cdot (\mathbf{x} - \mathbf{y}(s)) + |\mathbf{y}(s)|^2/4.$$

Hence $\partial RBP(s)$ is the circle with center $\mathbf{y}(s)/2$ and radius $|\mathbf{y}(s)|/2 = R/2$, and direct inspection shows that the points inside this circle lie outside the region of backprojection, so

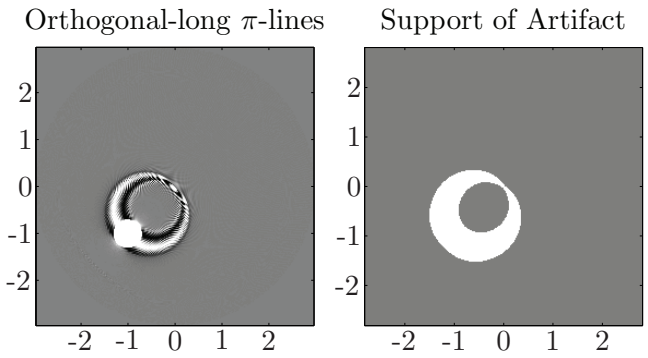

Figure 12. *Left: Comet tail artifact for orthogonal-long π-lines by (1.10). Reconstructed with formula (7.8) with $P = 2560$, $Q = 668$, $R = 3$, and $D = 6$. The image grayscale range is $[-8E-5, 8E-5]$. The reconstructed function is (7.11) with $\mathbf{x}_0 = (-1,-1)$, $a_1 = .3$, $a_2 = .3$, $m = 3$, and $\psi = 0$. Right: Support Γ of comet tail artifact predicted by Theorem 4.1.*

$RBP(s) \cap S_c = S_c \backslash D(s)$. A very similar argument applies for $\Gamma_{\mathbf{x}_0}$: According to Proposition 2.6 one has for $\mathbf{x} \neq \mathbf{0}$ that

$$\mathbf{x} \in \Gamma_{\mathbf{x}_0} \Leftrightarrow \mathbf{x}_0 \in L_\pi(\mathbf{x}) \Leftrightarrow \mathbf{x} \perp (\mathbf{x} - \mathbf{x}_0) \Leftrightarrow |\mathbf{x} - \mathbf{x}_0/2| = |\mathbf{x}_0|/2.$$

For ϵ positive and sufficiently small one observes that $\epsilon\mathbf{y}(s) \notin RBP(s)$ while $-\epsilon\mathbf{y}(s) \in RBP(s)$. Hence the point $\mathbf{x} = \mathbf{0}$ lies in $\partial RBP(s)$ for all s. It then follows from (2.1) that $\mathbf{0} \in \Gamma_{\mathbf{x}_0}$ for all $\mathbf{x}_0 \in S$. Finally, by definition, $\mathbf{0} \in RBP(s)$ for $s \in I_\pi(\mathbf{0}) = [-\pi/2, \pi/2]$. ■

For an alternative, entirely geometric proof for the set $\Gamma_{\mathbf{x}_0}$, see [5, Theorem 4.13].

Theorem 4.1 predicts that the support of the comet tail artifact for the orthogonal-long π-lines is a union of circles centered halfway between a point in the object and the origin. Figure 12 demonstrates that the artifact for the orthogonal-long π-lines is located where our theory predicts.

The orthogonal-long π-lines are a special case of the *tilted-long* π-lines where the radial ray through $\mathbf{x}$ and the π-line of $\mathbf{x}$ have a fixed angle of intersection ψ, $0 < \psi < \pi$, as shown in Figure 13. The tilted-long π-line of a point $\mathbf{x} \neq \mathbf{0}$ is the orthogonal-long π-line for the point $\mathbf{x}' = A\mathbf{x}$, where A is the matrix

$$A = \sin(\psi) \begin{bmatrix} \sin(\psi) & -\cos(\psi) \\ \cos(\psi) & \sin(\psi) \end{bmatrix}, \quad 0 < \psi < \pi; \tag{4.1}$$

see Figure 13. We derive $A\mathbf{x}$ as the rotation of $\mathbf{x}$ by $\psi - \pi/2$ and dilated by $\sin(\psi)$. For $\mathbf{x} = 0$ we define $I_\pi(\mathbf{0}) = [-\pi/2, \pi/2]$.

Corollary 4.3. *For the tilted-long family, one has $S_c = S\backslash\{\mathbf{0}\}$ and*

$$RBP(s) \cap S_c = \left\{ \mathbf{x} \in S_c : |\mathbf{x} - A^{-1}\mathbf{y}(s)/2| \geq \frac{R}{2\sin\psi} \right\}.$$

The set $\Gamma_{\mathbf{x}_0}$ is the intersection of S with the circle centered at $A^{-1}\mathbf{x}_0/2$ with radius $|A^{-1}\mathbf{x}_0/2| = |\mathbf{x}_0|/(2\sin\psi)$.

The exceptional point $\mathbf{x} = \mathbf{0}$ lies on $\partial RBP(s)$ for all s, in $RBP(s)$ for $s \in I_\pi(\mathbf{0}) = [-\pi/2, \pi/2]$, and in $\Gamma_{\mathbf{x}_0}$ for all $\mathbf{x}_0 \in S$.

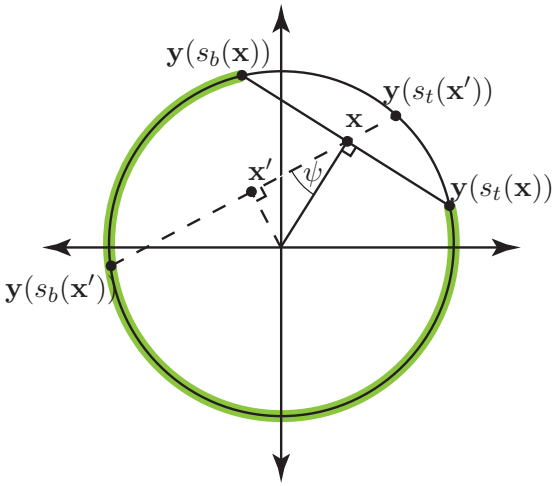

Figure 13. *Orthogonal-long and tilted-long π-lines.*

Proof. The corollary follows in a straightforward way from Theorem 4.1 by utilizing that the π-interval and π-line of $\mathbf{x}$ are the orthogonal-long π-interval and π-line of $A\mathbf{x}$, respectively, as well as the relation $A^T = \sin^2\psi A^{-1}$, which implies that $|A\mathbf{x} - \mathbf{b}| = \sin\psi\,|\mathbf{x} - A^{-1}\mathbf{b}|$. ∎

The final family of π-lines to be considered here are the *projected helix π-lines*. These are given by taking the corresponding values of s_b and s_t for the 3D helix and points in the $x_3 = 0$ plane, modulo 2π. That is, $s_b(\mathbf{x}) = s_b^H(\mathbf{x}) + 2\pi$, $s_t(\mathbf{x}) = s_t^H(\mathbf{x})$. Here the superscript ^{H} denotes the 3D helical case, and one identifies points in $S \subset \boldsymbol{R}^2$ with the corresponding points in the $x_3 = 0$ plane in $\boldsymbol{R}^3$. The radius of the helix is taken to be equal to the radius of the circle. For $\mathbf{x}$ in the $x_3 = 0$ plane, $s_t^H(\mathbf{x})$ and $s_b^H(\mathbf{x})$ are independent of the helix pitch [3]. Since $s_b(\mathbf{x}) > s_t(\mathbf{x})$, one has $I_\pi(\mathbf{x}) = [s_b(\mathbf{x}), 2\pi) \cup [0, s_t(\mathbf{x})]$ for all $\mathbf{x} \in S$. In particular, $0 \in I_\pi(\mathbf{x})$ for all $\mathbf{x} \in S$, so

$$RBP(0) = S.$$

For $s \neq 0$, one has

$$\begin{aligned} RBP(s) &= \{\mathbf{x} \in S : s \in I_\pi(\mathbf{x})\} \\ &= \{\mathbf{x} \in S : s + 2\pi k \in [s_b^H(\mathbf{x}), s_t^H(\mathbf{x})] \text{ for some integer } k\} \\ &= (RBP^H(s) \cup RBP^H(s - 2\pi)) \cap S. \end{aligned}$$

The region of backprojection can now be obtained from Proposition 3.2. Let

$$K_s(t) = \frac{1}{s - t}(s\mathbf{y}(t) - t\mathbf{y}(s)) \tag{4.2}$$

be the 2D analogue of the function $K_s(t)$ in Proposition 3.2. From (3.1) with $s_0 = 0$, one obtains

$$\partial RBP(s) \cap S = \{K_s(t) : s - 2\pi < t < 0\} \cup \{K_{s-2\pi}(t) : 0 < t < s\}, \quad s \neq 0. \tag{4.3}$$

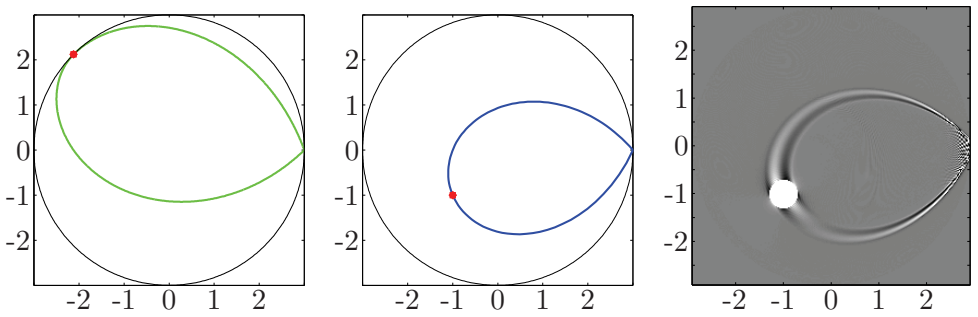

Figure 14. *Left: Boundary of the region of backprojection for the projected helix π-lines. The source circle of radius $R = 3$ is plotted in black and the source position $\mathbf{y}(3\pi/4)$ in red. The green curve is the boundary of $RBP(s)$ for $s = 3\pi/4$ as given by (4.3). The region of backprojection is the part of S exterior to this curve. Center: The set $\Gamma_{\mathbf{x}_0}$ (blue curve) for projected helix π-lines with $R = 3$ and $\mathbf{x}_0 = (-1, -1)$ according to (4.4). Right: Reconstruction of a smooth function centered at $\mathbf{x}_0$. The comet tail artifact appears at the location predicted by (2.2) and (4.4). The function and parameters for reconstruction and display are the same as those given in the caption of Figure 12.*

The two segments of the curve above share the same endpoints, namely $K_s(s - 2\pi) = \mathbf{y}(s) = K_{s-2\pi}(s)$ and $K_s(0) = \mathbf{y}(0) = K_{s-2\pi}(0)$. Hence, including these endpoints, (4.3) defines a closed curve. For $s = 3\pi/4$ this curve is shown in Figure 14 (left). The region of backprojection is the intersection of S with the exterior of this closed curve.

The parametrization of the curve $\partial RBP(s) \cap S$ used above also lends itself to determining the set $\Gamma_{\mathbf{x}_0}$ directly from its definition (2.1). Given some $\mathbf{x}_0 \in S$ one seeks for each $s \in [0, 2\pi)$ the point $\mathbf{x}_s \in \partial RBP(s) \cap S$ such that $\mathbf{x}_s, \mathbf{x}_0$ and $\mathbf{y}(s)$ are collinear. Rewriting $K_s(t)$ as $K_s(t) = \mathbf{y}(s) + \frac{s}{s-t}(\mathbf{y}(t) - \mathbf{y}(s))$ shows that $K_s(t)$ lies on the line through $\mathbf{y}(s)$ and $\mathbf{y}(t)$. The same holds true for $K_{s-2\pi}(t)$ and $K(_s(t - 2\pi)$ since $\mathbf{y}(s - 2\pi) = \mathbf{y}(s)$. Let $s^* = s^*(s, \mathbf{x}_0)$ be such that $\mathbf{y}(s^*)$, $\mathbf{x}_0$, and $\mathbf{y}(s)$ are collinear. From (4.3) it now follows that

$$\mathbf{x}_s = \begin{cases} K_s(s^* - 2\pi) & \text{if } s < s^* < 2\pi, \\ K_{s-2\pi}(s^*) & \text{if } 0 < s^* < s. \end{cases}$$

It is well known in fan-beam tomography that $s^* = (s - 2\alpha^*(s, \mathbf{x}_0) + \pi)$ modulo 2π, with $\alpha^*(s, \mathbf{x}_0)$ being the fan-angle of the ray with vertex $\mathbf{y}(s)$ that passes through $\mathbf{x}_0$; see (7.6). In Figure 4 one has $s_b(\mathbf{x}) = s^*(0, \mathbf{x})$. It can be seen from Figure 4 that $s^*(s, \mathbf{x}_0) > s$ for $0 < s < s^*(0, \mathbf{x}_0)$ and $0 < s^*(s, \mathbf{x}_0) < s$ for $s^*(0, \mathbf{x}_0) < s < 2\pi$. Hence

$$\mathbf{x}_s = \begin{cases} K_s(s^* - 2\pi) & \text{if } 0 < s < s^*(0, \mathbf{x}_0), \\ K_{s-2\pi}(s^*) & \text{if } s^*(0, \mathbf{x}_0) < 2 < 2\pi. \end{cases}$$

Furthermore, if $s_1 \geq s^*(0, \mathbf{x}_0)$, then $s_1 = s^*(s, \mathbf{x}_0)$ for some $s \in [0, s^*(0, \mathbf{x}_0))$ and $s_1^* = s^*(s_1, \mathbf{x}_0) = s$. It follows that

$$\mathbf{x}_{s_1} = K_{s_1-2\pi}(s_1^*) = K_{s_1-2\pi}(s) = K_s(s_1 - 2\pi) = K_s(s^* - 2\pi) = \mathbf{x}_s.$$

It therefore suffices to determine $\mathbf{x}_s$ for $0 \leq s < s^*(0, \mathbf{x}_0)$. This gives

$$\Gamma_{\mathbf{x}_0} = \{K_s(s^*) : 0 \leq s < \pi - 2\alpha^*(0, \mathbf{x}_0)\}, \text{ where } s^* = s - 2\alpha^*(s, \mathbf{x}_0) + \pi. \tag{4.4}$$

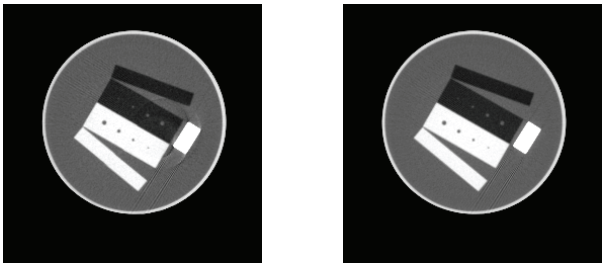

Figure 15. *Reconstruction of a calibration phantom from real data. Source radius $R = 2.868$, $P = 720$ source positions, 512 equispaced detectors with $\Delta\alpha = \arcsin(1/R)/256$. Center of rotation assumed at detector 257. Left: Reconstruction with the π-line formula (7.5) and orthogonal-long π-lines. A comet tail artifact is visible near the small bright block. Right: Reconstruction from the same data set using formula (7.9), which is not a π-line formula. No comet tail artifact appears.*

Figure 14 (center) shows $\Gamma_{\mathbf{x}_0}$ for $R = 3$ and $\mathbf{x}_0 = (-1\ -1)$. The numerical experiment shown in Figure 14 (right) confirms that the comet tail artifact appears at the location given by (4.4) and (2.2).

5. Misalignment of projection data and comet tail artifacts. In [3, section 7] we compared the performance of 2D reconstruction algorithms based on the 2D version of (1.10) in the form (7.5) with reconstructions from formula (7.9) and the standard filtered backprojection algorithm as described, for example, in [8]. The latter two methods are not based on π-line formulas. Our conclusion from these experiments was that for objects with stronger singularities the reconstructions based on (7.5) showed artifacts that the other two algorithms did not exhibit. Figure 15 shows one of these experiments, consisting of reconstructions of a calibration phantom from real data using (7.5) and (7.9), respectively. In the reconstruction from (7.5) a comet tail artifact emerging from the small bright block is visible that is absent in the other image. It is the purpose of this section to show that these artifacts stem from a particular sensitivity of the π-line reconstructions to even small misalignments in the measured data with respect to the fan-angle α, and that better reconstructions are obtained if data alignment is properly accounted for. Furthermore, we will demonstrate that this sensitivity can be used in some cases to determine the correct alignment of a data set.

Suppose that our measured x-ray data $g(s,\alpha)$ (cf. (7.4)) has a uniform shift in the α coordinate. That is, for some $t \in \mathbb{R}$ we have $g_t(s,\alpha) = g(s,\alpha+t)$. We now investigate the effect of this misalignment by means of a linearization. Let $f_t(\mathbf{x})$ be the reconstruction from the data g_t and assume that we have sufficiently smooth data $g(s,\alpha)$. Then a Taylor expansion with respect to α yields

$$g_t(s,\alpha) \simeq g(s,\alpha) + t\frac{\partial g}{\partial \alpha}(s,\alpha). \tag{5.1}$$

The reconstruction error $e(t) = f(\mathbf{x}) - f_t(\mathbf{x})$ caused by the data misalignment is approximately given by

$$e(t) \approx -\frac{t}{2\pi^2}\int_{I_\pi(\mathbf{x})}\frac{1}{|\mathbf{x}-\mathbf{y}(s)|}\int_0^{2\pi}\left(\frac{\partial}{\partial\alpha}\frac{\partial g}{\partial s}(s,\alpha)+\frac{\partial^2 g}{\partial\alpha^2}(s,\alpha)\right)k(\alpha^*-\alpha)\,d\alpha\,ds,$$

where $k(\alpha) = 1/\sin(\alpha)$. An integration by parts with respect to α yields

$$e(t) \approx -\frac{t}{2\pi^2} \int_{I_\pi(\mathbf{x})} \frac{1}{|\mathbf{x} - \mathbf{y}(s)|} \int_0^{2\pi} \left(\frac{\partial g}{\partial s}(s,\alpha) + \frac{\partial g}{\partial \alpha}(s,\alpha) \right) k'(\alpha^* - \alpha)\, d\alpha\, ds. \tag{5.2}$$

This formula has the same structure as the reconstruction formula (7.5) but with a different convolution kernel. This new kernel can be discretized, for example, by differentiating the band-limited kernel (7.7), which gives

$$k'(\alpha) \approx \frac{b\sin(b\alpha)}{\sin(\alpha)} - \frac{(1 - \cos(b\alpha))\cos(\alpha)}{\sin^2(\alpha)}, \tag{5.3}$$

where b is the cut-off frequency.

As seen in the upper four images in Figure 16, the approximate error term for $e(t)$, (5.2), and $e(t)$ contain the comet tail artifacts found in the calibration phantom reconstruction and thus confirm that data misalignment causes strong comet tail artifacts when the reconstruction is performed with a π-line reconstruction formula. The images of (5.2) and $e(t)$ are very similar and thus validate the approximation used in (5.1). The comet tail artifact varies with the selection of the family of π-lines and appears in the locations predicted by Theorem 4.1 and (4.4), respectively. The bottom two images in Figure 16 show that these distinctive comet tail artifacts are absent in reconstructions with formula (7.9), which is not a π-line formula. Of course, in the case of a sizeable misalignment of $t \simeq 0.8\Delta\alpha$ as shown in Figure 16, there are other strong artifacts besides the comet tail artifact.

The presence of the comet tail artifact in the reconstruction from formula (7.5) shown in Figure 15 suggests that the assumed alignment of the α coordinate of the x-ray data may be inaccurate. Our experiments have shown that the comet tail artifact is not nearly as strong with well-aligned projection data of discontinuous functions. The comet tail artifact resulting from misaligned data is of the same order of magnitude as the density values of the function and thus is a leading source of error. However, the high sensitivity with regard to alignment may be used to determine the correct alignment. Figure 17 (left) shows a graph of the TV norm of a subregion of the reconstructed image as a function of a shift in α. Here the shifts vary between $-\Delta\alpha$ and $\Delta\alpha$. The minimum occurs at a shift of $0.19\,\Delta\alpha$. Figure 17 (right) shows a reconstruction with this shift taken into account. The comet tail artifact is much reduced. While these results are an encouraging proof of concept, further development of this method for misalignment correction will be the subject of future research. For a recent alternative method for misalignment correction, see [10].

6. Conclusion. We have investigated two distinctive features of π-line reconstruction formulas, the region of backprojection and the comet tail artifact. Our results provide new insights into the behavior of π-line reconstruction formulas and are independent of the detector geometry. General properties of the boundary of the region of backprojection were proved and applied in two and three dimensions. While the π-lines for the helix are uniquely determined, there is great flexibility to choose a family of π-lines in the 2D case. Useful properties of the family of π-lines, such as being nonintersecting and/or boundary-regular, were identified and shown to lead to a simplification of the theory. The general theory was used to identify the region of backprojection for the helix as well as for a representative collection of

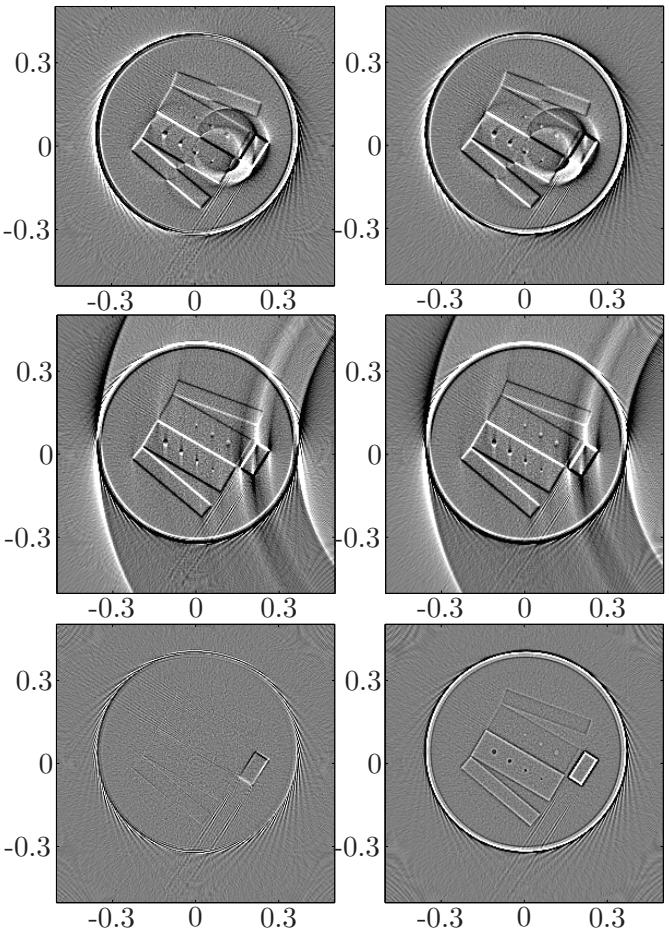

Figure 16. *Top left: Approximate error term (5.2) for $e(t)$ with orthogonal-long π-lines. Top right: Actual error term $e(t)$ with orthogonal-long π-lines. Center left: Approximate error term (5.2) for $e(t)$ with helical π-lines. Center right: Actual error term $e(t)$ with helical π-lines. Bottom left: Approximate error term for reconstruction formula (7.9) which is not a π-line formula. Bottom right: Actual error term for reconstruction with (7.9). For all six images images the data misalignment t is equal to 0.8 times the detector width, the source radius is $R = 2.868$, and the images are displayed in the square $[-0.5, 0.5]^2$. The reconstructions based on (7.9) are included to better distinguish the comet tail artifact from other errors caused by the misalignment.*

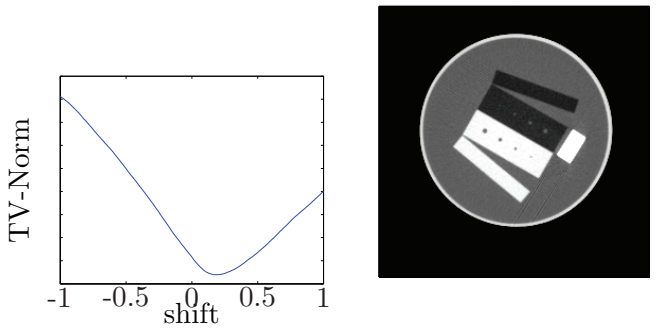

Figure 17. *Calibration phantom.*

2D families of π-lines. In the case of the helix the simple structure of the region of backprojection and its boundary was most clearly apparent when considering its intersections with surfaces of π-lines called chips instead of horizontal planes.

A heuristic principle relating the comet tail artifact to the boundary of the region of backprojection was proposed, then reformulated to be expressed in terms of π-lines, and finally validated with a variety of numerical examples which confirmed that the theory correctly determines the location of the artifact. It was also shown that the proposed support of the artifact contains the support of the Hilbert image $g(\mathbf{x}) = H_{\boldsymbol{\beta}(s_t(\mathbf{x}),\mathbf{x})} f(\mathbf{x})$. We reiterate that the comet tail artifact is usually small and does not significantly degrade the image.

One could ask whether in two dimensions π-line reconstruction formulas may have any particular advantages, for example when compared to the conventional fan-beam filtered backprojection algorithm as described in [8], or to reconstructions from formula (7.9). One such situation occurs when the x-ray source is very close to the object. Then the conventional algorithm as well as reconstruction algorithms based on (7.9) show artifacts in the parts of the reconstruction region that are near the source curve. A π-line reconstruction formula where the region of backprojection $RBP(s)$ does not contain points close to the source position $\mathbf{y}(s)$ mitigates this problem and therefore is advantageous. The optimal family of π-lines for this purpose appear to be the orthogonal-long π-lines, but the effect can also be seen in Figure 14. The left part of the figure shows that for $s \neq 0$ most points in the vicinity of $\mathbf{y}(s)$ lie outside the region of backprojection. This is not the case for $s = 0$, however, since for the projected helix π-lines $RBP(0) = S$. Accordingly, the right image of the figure shows an additional oscillatory artifact near the point $\mathbf{y}(0) = (3, 0)$ at the right boundary of the image, while there is no such artifact near the source curve in other parts of the image.

A possible drawback of π-line reconstruction formulas is a relatively strong sensitivity to misaligned data, which leads to a large comet tail artifact that does degrade the image. On the other hand, we demonstrated the potential to use this sensitivity to find the correct alignment. Using a linearization, we also derived an error term that reproduces the location of the artifact.

7. Remarks on the numerical implementation. The discretization and numerical implementation of (1.10) used in the numerical experiments presented in this paper are as described in [3] and [14]. The source code for some of the experiments is available from the authors upon request. In this section we give a brief summary for completeness and as background for section 5.

For the 3D case we introduce a coordinate system that rotates with the source and is given by the three unit vectors

$$\mathbf{e}_u(s) = (-\sin s, \cos s, 0), \quad \mathbf{e}_v(s) = -(\cos s, \sin s, 0), \quad \mathbf{e}_w = (0, 0, 1). \tag{7.1}$$

The source curve (1.1) can then be written as

$$\mathbf{y}(s) = -R\mathbf{e}_v + hs\mathbf{e}_w. \tag{7.2}$$

For our numerical implementation we used a measurement geometry with a curved detector array where x-rays that are emitted from a source at $\mathbf{y}(s)$ and pass through the object are

recorded by detectors located on the rotating curved surface

$$\mathbf{d}(s,\alpha,w) = \mathbf{y}(s) + D\sin\alpha\,\mathbf{e}_u + D\cos\alpha\,\mathbf{e}_v + w\,\mathbf{e}_w, \quad |\alpha| \le \alpha_{max}, \quad |w| \le w_{max}, \quad D \ge R. \tag{7.3}$$

Geometrically, D is the distance between $\mathbf{y}(s)$ and the surface $\mathbf{d}(s,\cdot,\cdot)$, α is the angle between $\mathbf{e}_v$ and the projection onto the $x_3 = 0$ plane of the ray connecting the source $\mathbf{y}(s)$ with a detector located at $\mathbf{d}(s,\alpha,w)$, and w is the difference between the x_3 coordinates of the detector position $\mathbf{d}(s,\alpha,w)$ and the source position $\mathbf{y}(s)$.

The measured data are then given by

$$g(s,\alpha,w) = \mathcal{D}f(\mathbf{y}(s), \boldsymbol{\theta}(s,\alpha,w))$$

with $\mathbf{y}(s)$ as in (7.2) and

$$\boldsymbol{\theta}(s,\alpha,w) = \frac{1}{\sqrt{D^2+w^2}}\left(D\sin\alpha\,\mathbf{e}_u + D\cos\alpha\,\mathbf{e}_v + w\,\mathbf{e}_w\right).$$

We have P source positions per turn with $\Delta s = 2\pi/P$ and $Q = 2q$ x-rays measured uniformly over the angular range $\alpha \in [-\pi/2, \pi/2]$. That is, we have $2q$ discrete angular measurements for $\alpha_l = l\Delta\alpha$ for $l = -q, \ldots, q-1$ with $\Delta\alpha = \pi/Q$. The variable w is discretized with a step size $\Delta w = D\Delta\alpha$.

The corresponding expressions for the 2D case can be obtained by setting $w = 0$ and using the circle (1.2), i.e., $\mathbf{y}(s) = -R\mathbf{e}_v$, as the source curve. This gives

$$g(s,\alpha) = \mathcal{D}f(\mathbf{y}(s), \boldsymbol{\theta}(s,\alpha)), \quad \boldsymbol{\theta}(s,\alpha) = \sin\alpha\,\mathbf{e}_u + \cos\alpha\,\mathbf{e}_v. \tag{7.4}$$

Expressed with respect to the detector coordinates (s, α), the 2D version of the reconstruction formula (1.10) now reads as

$$f(\mathbf{x}) = \frac{1}{2\pi^2}\int_{I_\pi(\mathbf{x})} \frac{1}{|\mathbf{x}-\mathbf{y}(s)|}\int_0^{2\pi}\left(\frac{\partial g(s,\alpha)}{\partial s} + \frac{\partial g(s,\alpha)}{\partial \alpha}\right)\frac{d\alpha\,ds}{\sin(\alpha^*-\alpha)} \tag{7.5}$$

with $\mathbf{x} = (x_1, x_2, 0)$ and (s, α^*) being the detector coordinates for the ray from the source position $\mathbf{y}(s)$ that passes through the point $\mathbf{x}$,

$$\alpha^*(s,\mathbf{x}) = \arctan\left(\frac{\boldsymbol{\beta}\cdot\mathbf{e}_u}{\boldsymbol{\beta}\cdot\mathbf{e}_v}\right) \tag{7.6}$$

with $\boldsymbol{\beta} = \boldsymbol{\beta}(s,\mathbf{x})$ given by (1.8) and $\mathbf{e}_u$, $\mathbf{e}_v$ by (7.1) with the third component omitted.

In practice the singular convolution kernel $1/\sin(\alpha)$ is regularized by an approximation $k(\alpha)$, e.g.,

$$k(\alpha) = \frac{1-\cos(b\alpha)}{\sin(\alpha)}, \tag{7.7}$$

where b is a cut-off frequency that is chosen according to the sampling density and noisiness of the data. This gives the approximate reconstruction formula

$$f(\mathbf{x}) \simeq \frac{1}{2\pi^2}\int_{I_\pi(\mathbf{x})} \frac{1}{|\mathbf{x}-\mathbf{y}(s)|}\int_0^{2\pi}\left(\frac{\partial g(s,\alpha)}{\partial s} + \frac{\partial g(s,\alpha)}{\partial \alpha}\right)k(\alpha^*-\alpha)\,d\alpha\,ds \tag{7.8}$$

which is of filtered backprojection type.

The discrete implementation of the backprojection with the trapezoidal rule requires an interpolation at the endpoints of $I_\pi(\mathbf{x})$. This interpolation was implemented according to formulas (63) and (64) in [14].

For a given point $\mathbf{x}$ the π-line segment connecting $\mathbf{y}(s_b(\mathbf{x}))$ and $\mathbf{y}(s_t(\mathbf{x}))$ divides the circle $\mathbf{y} = R$ into two arcs. In (7.5) and (7.8) the integration in s from $s_b(\mathbf{x})$ to $s_t(\mathbf{x})$ involves only one of the arcs. It would be equally valid to interchange the roles of s_b and s_t and integrate over the other arc. Averaging the two possibilities gives the inversion formula

$$f(\mathbf{x}) = \frac{1}{4\pi^2}\int_0^{2\pi}\frac{1}{|\mathbf{x}-\mathbf{y}(s)|}\int_0^{2\pi}\left(\frac{\partial g(s,\alpha)}{\partial s}+\frac{\partial g(s,\alpha)}{\partial \alpha}\right)\frac{1}{\sin(\alpha^*-\alpha)}\,d\alpha\,ds, \tag{7.9}$$

which is no longer a π-line reconstruction formula and was first found in [6]. For further details see [3, 17].

We use the following family of functions to construct mathematical phantoms for our numerical experiments:

$$b_m(\mathbf{x}) = \left(1-|\mathbf{x}|^2\right)_+^m = \begin{cases} \left(1-|\mathbf{x}|^2\right)^m & \text{if } 1-|\mathbf{x}|^2 \geq 0, \\ 0 & \text{if } 1-|\mathbf{x}|^2 < 0. \end{cases} \tag{7.10}$$

Here m is a parameter that controls the smoothness of the function. Usually we choose either $m = 3$, which gives a smooth function, or $m = 0$, which yields the characteristic function of the unit ball. Our object function is then given by linear combinations of functions of the form

$$f(\mathbf{x}) = b_m(T(\mathbf{x}-\mathbf{x}_0)) \tag{7.11}$$

with

$$T = \begin{bmatrix} \cos(\psi)/a_1 & \sin(\psi)/a_1 & 0 \\ -\sin(\psi)/a_2 & \cos(\psi)/a_2 & 0 \\ 0 & 0 & 1/a_3 \end{bmatrix}.$$

For the 2D case we omit the third row and column of the matrix T.

REFERENCES

[1] M. Defrise, F. Noo, R. Clackdoyle, and H. Kudo, *Truncated Hilbert transform and image reconstruction from limited tomographic data*, Inverse Problems, 22 (2006), pp. 1037–1053.

[2] M. Defrise, F. Noo, and H. Kudo, *A solution to the long-object problem in helical cone-beam tomography*, Phys. Med. Biol., 45 (2000), pp. 623–643.

[3] A. Faridani, R. Hass, and D. C. Solmon, *Numerical and theoretical explorations in helical and fan-beam tomography*, J. Phys.: Conf. Ser., 124 (2008), 012024.

[4] I. M. Gelfand and M. I. Graev, *Crofton function and inversion formulas in real integral geometry*, Funct. Anal. Appl., 25 (1991), pp. 1–5.

[5] R. A. Hass, *π-Line Reconstruction Formulas in Computed Tomography*, Ph.D. thesis, Department of Mathematics, Oregon State University, Corvallis, OR, 2009.

[6] G. T. Herman and A. Naparstek, *Fast image reconstruction based on a Radon inversion formula appropriate for rapidly collected data*, SIAM J. Appl. Math., 33 (1977), pp. 511–533.

[7] S. H. Izen, *A fast algorithm to compute the π-line through points inside a helix cylinder*, Proc. Amer. Math. Soc., 135 (2007), pp. 269–276.

[8] A. C. Kak and M. Slaney, *Principles of Computerized Tomographic Imaging*, IEEE Press, New York, 1988.
[9] A. Katsevich, *An improved exact filtered backprojection algorithm for spiral computed tomography*, Adv. in Appl. Math., 32 (2004), pp. 681–697.
[10] A. Katsevich, M. Silver, and A. Zamyatin, *Local tomography and the motion estimation problem*, SIAM J. Imaging Sci., 4 (2011), pp. 200–219.
[11] M. Kapralov and A. Katsevich *A study of* 1*PI algorithms for a general class of curves*, SIAM J. Imaging Sci., 1 (2008), pp. 418–459.
[12] F. Noo, R. Clackdoyle, and J. D. Pack *A two-step Hilbert transform method for* 2*D image reconstruction*, Phys. Med. Biol., 49 (2004), pp. 3903–3923.
[13] F. Noo, M. Defrise, R. Clackdoyle, and H. Kudo, *Image reconstruction from fan-beam projections on less than a short scan*, Phys. Med. Biol., 47 (2002), pp. 2525–2546.
[14] F. Noo, J. Pack, and D. Heuscher, *Exact helical reconstruction using native cone-beam geometries*, Phys. Med. Biol., 48 (2003), pp. 3787–3818.
[15] H. Turbell and P. E. Danielsson, *An improved PI-method for reconstruction from helical cone-beam projections*, in 1999 IEEE Nuclear Science Symposium. Conference Record, 1999, pp. 865–868.
[16] Y. Ye, S. Zhao, H. Yu, and G. Wang, *A general exact reconstruction for cone-beam CT via backprojection-filtration*, IEEE Trans. Med. Imaging, 24 (2005), pp. 1190–1198.
[17] J. You and G. L. Zeng, *Hilbert transform based FBP algorithm for fan-beam CT full and partial scans*, IEEE Trans. Med. Imaging, 26 (2007), pp. 190–199.
[18] Y. Zou and X. C. Pan, *An extended data function and its generalized backprojection for image reconstruction in helical cone-beam CT*, Phys. Med. Biol., 49 (2004), pp. N383–N387.
[19] Y. Zou and X. Pan, *Exact image reconstruction on PI-lines from minimum data in helical cone-beam CT*, Phys. Med. Biol., 49 (2004), pp. 941–959.
[20] Y. Zou, X. Pan, and E. Y. Sidky, *Image reconstruction in regions-of-interest from truncated projections in a reduced fan-beam scan*, Phys. Med. Biol., 50 (2004), pp. 13–27.